Numerical study of failure behaviour of pre-cracked rock specimens under conventional triaxial compression

CrossMark

S.Y. Wang [a,*], S.W. Sloan [a], D.C. Sheng [a], S.Q. Yang [b], C.A. Tang [c]

[a] ARC Centre of Excellence for Geotechnical Science and Engineering, Civil, Surveying and Environmental Engineering, The University of Newcastle, Callaghan, NSW 2308, Australia
[b] State Key Laboratory for Geomechanics and Deep Underground Engineering, School of Mechanics and Civil Engineering, China University of Mining and Technology, Xuzhou 221008, PR China
[c] School of Civil & Hydraulic Engineering, Dalian University of Technology, Dalian 116024, PR China

ABSTRACT

Macroscopic pre-existing flaws play an important role in evaluating the strength and the failure modes of a heterogeneous rock mass. Crack initiation, propagation and coalescence from macroscopic pre-existing flaws are considered in a 3-D numerical model (RFPA3D) to investigate their effects on the underlying failure modes of rock. A feature of the code RFPA3D is that it can numerically simulate the evolution of cracks in three-dimensional space, as well as the heterogeneity of the rock mass. Three types of flaw geometries were evaluated numerically against experimental results: Type A for intact specimen, and Types B and C for flawed cylindrical specimens with different macroscopic pre-existing flaws, respectively. The effect of confining pressure on the fracture evolution was also considered. Numerical results showed that both the ligament angle and the flaw angle of two pre-existing cracks can affect the uniaxial compressive strength of the specimen and the mechanism of fracture evolution. In addition, both the uniaxial compressive strength and the accumulated acoustic emission increase with increasing heterogeneity.

1. Introduction

Rock is a heterogeneous geo-material, with many pre-existing fractures varying from microscopic cracks to macroscopic joints and even to continental faults. When rock mass is subjected to different types of loading, fractures can initiate and propagate from these pre-existing cracks or pores, and then coalescence into macro-failure of rock. Usually, in uniaxial compression, three basic kinds of failure modes of rock can be observed. They are splitting, spalling, and oblique failure (Germanovich et al., 1994). Splitting and spalling are actually tensile failure, whereas oblique failure appears like shear failure. Certainly, all these failure modes can be observed at the macro scale. However, at the micro scale, the three macro failure modes are the results of interaction between micro-cracks (Griffith, 1924). Micro-cracks can be tensile cracks or shear cracks, depending on the local stress distribution within the rock specimen. In addition, for biaxial loading, the confining pressure can hamper the growth of tensile cracks and thus cause the growth of smaller and more densely distributed pre-existing cracks. This can result in localization and shear fractures in the brittle regime. The interaction of these localised shear fractures can initiate macro-failure of the rock specimen. Healy et al. (2006a, 2006b) provided a micromechanical model to explain how brittle shear fractures can form obliquely to all three remote principal stresses.

Many researchers have studied the mechanism of two-dimensional fracture evolution from pre-existing flaw(s) (Brace and Bombolakis, 1963; Hoek and Bieniawski, 1965; Horii and Nemat-Nasser, 1985, 1986; Ashby and Hallam, 1986; Bobet, 1997, 2000; Bobet and Einstein, 1998; Zhu et al., 1998; Wong and Chau, 1998; Vasarhelyi and Bobet, 2000). Basically, two secondary tensile cracks initiate from both ends of the inclined flaw(s), and propagate in a stable manner towards the major axis of compression. Wong et al. (2001) studied the mechanism of crack interaction in specimens with three parallel flaws, and results showed that the arrangement of the flaws played an important role in the coalescence of cracks. However, most studies on mechanisms of brittle rock fracturing in compression have been limited to cracks in two dimensions. For three-dimensional specimens, tensile cracks or shear cracks occur on 3-D faces, makes the evolution mechanism much more complicated (Yang et al., 2012a,b).

Huang and Wong (2007) carried out a series of uniaxial compressive tests on polymethly methacrylate (PMMA) with pre-existing 3D flaws. Their experimental results showed that

* Corresponding author. Tel.: +61 2 4921 5745; fax: +61 2 4921 6991.
  E-mail addresses: Shanyong.Wang@newcastle.edu.au (S.Y. Wang), Scott.Sloan@newcastle.edu.au (S.W. Sloan), Daichao.Sheng@newcastle.edu.au (D.C. Sheng), yangsqi@hotmail.com (S.Q. Yang), catang@mechsoft.cn (C.A. Tang).

interaction of distinct cracks could either promote or restrain the evolution of cracks in 3D space. Yang et al. (2008) conducted a series of experimental tests on cylindrical marble specimens with two macroscopic pre-existing flaws. They observed three failure types: a tensile mode, a shear mode, and a mixed mode (which is a combination of the tensile and shear modes). These failure modes depend on the heterogeneity of the marble, the arrangement of macroscopic pre-existing flaws, and the confining pressure. Usually, the confining pressure can restrain the development of shear cracks. However, for laboratory tests, it is difficult to determine the heterogeneity of intact rock in specimens. Due to this inherent heterogeneity and the end-boundary conditions, the resulting stresses within a cylindrical sample are inevitably non-uniform on the micro-scale. As it is difficult to know the stress distribution within a specimen during the loading process, it is not possible to predict the orientation of the initiation of cracks *a priori*.

Numerical models can be used to determine the stress distribution within laboratory specimens, and hence predict and simulate the evolution of cracks. Based on experimental creep tests, a phenomenological model was presented by Kaiser and Morgenstern (1981) to investigate the time-dependent deformation and failure mechanisms of rock masses. Schlangen and Van Mier (1992) were the first to apply lattice models for simulating progressive failure in concrete. Place and Mora (1999) developed a particle-based lattice model to study the physics of rocks and the nonlinear dynamics of earthquake. Shen and Stephansson (1993) developed the displacement discontinuity method, using a modified G-criterion, to numerically simulate the crack propagation and coalescence between two open/closed macroscopic pre-existing flaws. Fanella and Krajcinovic (1988) proposed a micromechanical damage model for concrete subject to compression. The overall non-linear response of the material is attributed solely to the growth of the randomly oriented microcracks which are located on the aggregate-cement paste interfaces. The results generated from this model were in good agreement with the experimentally observed trends, even though a few assumptions were introduced to make the calculation less complex. Blair and Cook (1998) developed a statistical model, which is called non-linear rule-based model, and coupled it with the boundary element method. The effect of microscale heterogeneity on macroscopic deformation was researched using the model. Vasarhelyi and Bobet (2000) reported the displacement discontinuity method, FROCK, and numerically simulated the initiation, propagation and coalescence of cracks between two macroscopic pre-existing flaws under uniaxial compression. Their numerical predictions were in good agreement with their experimental results.

In addition, the discrete fibre-bundle model was provided by Turcotte et al. (2003) to study the brittle failure of a solid. This discrete, microscopic fibre-bundle model can give exactly the same solution for material failure by continuum, macroscopic damage model. A pore crack model was developed by Sammis and Ashby (1986) to investigate the interaction of growing cracks with a spherical pore. This approach to crack-pore interaction is in agreement with observations. Feng et al. (2006) simulated the failure process of heterogeneous rocks successfully by using elastoplastic cellular automata. Based on static fatigue laws, Amitrano and Helmstetter (2006) proposed a numerical model to study the time-dependent damage and deformation of rocks under creep. Using a different approach, RFPA2D was developed to investigate the failure process of rock mass (Tang, 1997; Tang and Kou, 1998; Tang et al., 2001; Wang et al., 2006, 2009, 2011a,b, 2012a,b; Xu et al., 2012; Li et al., 2012a,b,c). In this code, the Weibull distribution function was introduced to describe the heterogeneity of rock mass. This code can be used to simulate the non-linear deformation, stress distribution, initiation and growth of cracks and fractures in heterogeneous materials (Tang and Kou, 1998; Tang et al., 2001; Wang et al., 2012a). Brantut et al. (2013) provided a good review and summary of existing typical models for time-dependent cracking and brittle creep in crustal rocks in details. However, most of these numerical models were limited to 2-D situations and the evolution of cracks in the specimen was not well captured.

In this study, the code RFPA3D, which is an extension of RFPA2D, is applied to investigate the 3D fracturing processes of cylindrical rock specimens with two macroscopic pre-existing flaws. First, the numerical method, RFPA3D, is introduced briefly. Three types of flaw geometries, i.e. Type A for an intact specimen, and Types B and C for flawed cylindrical specimens with different macroscopic pre-existing flaws, are simulated numerically and the results are evaluated against experimental observations. The study also investigates the effect of the confining pressure on the fracture evolution, as well as the effects of both the ligament angle and the flaw angle of pre-existing cracks on the uniaxial compressive strength of a specimen. Finally, the influence of both the heterogeneity index (m) on the uniaxial compressive strength, and the accumulated acoustic emission (AE) on the crack evolution patterns, are considered.

2. Brief description of RFPA3D

In RFPA3D, it is assumed that the domain consists of elements with the same shape and size and that there is no geometric priority in any orientation (Tang, 1997; Wang et al., 2006). The statistical distribution of the elemental mechanical parameters is described by the Weibull distribution function (Weibull, 1951). These elemental mechanical parameters include the uniaxial compressive strength, the elastic modulus and Poisson's ratio. The Weibull distribution function is as follows (Weibull, 1951):

$$W(x) = \frac{m}{x_0}\left(\frac{x}{x_0}\right)^{m-1}\exp\left[-\left(\frac{x}{x_0}\right)^m\right] \tag{1}$$

where x is a given mechanical property (such as the strength or elastic modulus); x_0 is a scale parameter; and m is a parameter that defines the shape of the distribution function. In the present study, the parameter m defines the degree of material homogeneity and is thus referred to as the homogeneity index (Tang, 1997). As the homogeneity index increases, the material becomes more homogeneous.
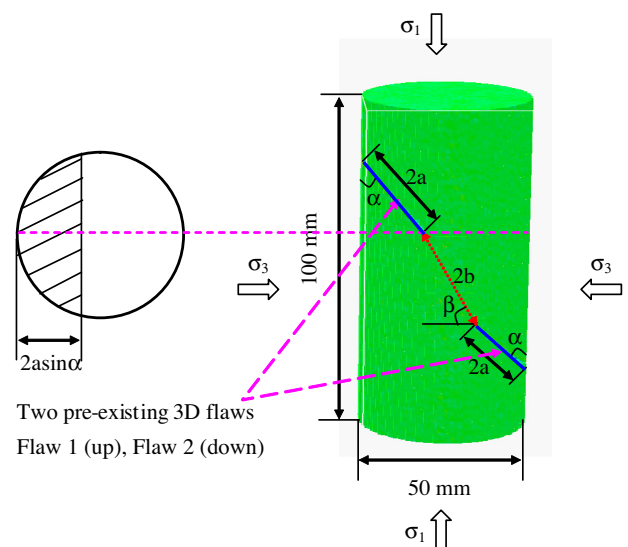

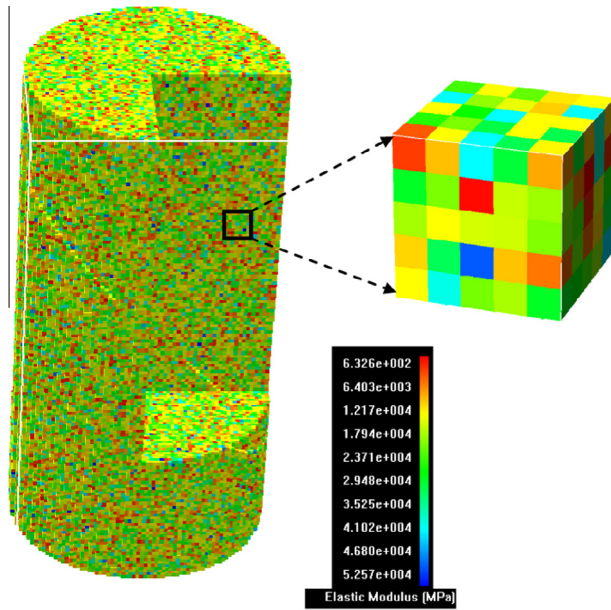**Fig. 1.** Numerical model with two pre-existing 3D flaws.

Fig. 2. 3D mesh distribution in the numerical model.

Each of the element material properties is different and is specified according to the Weibull distribution. In fact, m accounts for flaws on the microscale (cracks and pores), i.e. the heterogeneity of material in microscale.

In addition, the approach of damage mechanics is employed to model the mechanical behaviour of meso-scale elements. For each element, the material is assumed to be linear elastic, isotropic and damage-free before loading, with its elastic properties defined by the elastic modulus and Poisson's ratio. After the initiation of damage, the elastic modulus of an element is supposed to degrade monotonically as the damage evolves according to the relation (Tang et al., 2007; Wang et al., 2011a):

$$E = (1 - D)E_0 \tag{2}$$

where D represents the damage variable; and E and E_0 are the elastic modulus of the damaged and the undamaged material, respectively.

The constitutive relationship of a mesoscopic element under uniaxial tension is expressed as (Zhu and Tang, 2006):

$$D = \begin{cases} 0 & \varepsilon < \varepsilon_{t0} \\ 1 - \frac{f_{tr}}{E_0 \varepsilon} & \varepsilon_{t0} \leqslant \varepsilon \leqslant \varepsilon_{tu} \\ 1 & \varepsilon > \varepsilon_{tu} \end{cases} \tag{3}$$

where f_{tr} is the residual tensile strength, which is given as $f_{tr} = \lambda f_{t0} = \lambda E_0 \varepsilon_{t0}$; f_{t0} and λ are the uniaxial tensile strength and residual strength coefficients, respectively; ε_{t0} is the strain at the elastic limit, which can be called the threshold strain; and ε_{tu} is the ultimate tensile strain at which the element would be completely damaged. The ultimate tensile strain is defined as $\varepsilon_{tu} = \eta \varepsilon_{t0}$, where η is the ultimate strain coefficient. Eq. (3) can also be expressed as (Zhu and Tang, 2006; Wang et al., 2011a):

Table 1
Pre-existing crack geometries of flawed specimens (Yang et al., 2008) (Case I).

Homogeneity index (m)	Flaw geometry	Flaw angle (α/°)	Ligament angle (β/°)	Flaw length (2a/mm)	Ligament length (2b/mm)	σ_3/MPa
2	Type A	N/A	N/A	N/A	N/A	0
		N/A	N/A	N/A	N/A	5
1.5	Type B	30	38	24	33	0
	Type C	45	61	24	33	0

Table 2
Pre-existing crack geometries of flawed specimens with three different ligament angles (β) (Case II).

Homogeneity index (m)	Flaw angle (α/°)	Ligament angle (β/°)	Flaw length (2a/mm)	Ligament length (2b/mm)	σ_3/MPa
2	30	45	24	33	0
	30	60	24	33	0
	30	75	24	33	0

Table 3
Pre-existing crack geometries of flawed specimens with three different flaw angle (α) (Case II).

Homogeneity index (m)	Flaw angle (α/°)	Ligament angle (β/°)	Flaw length (2a/mm)	Ligament length (2b/mm)	σ_3/MPa
2	30	75	24	33	0
	45	75	24	33	0
	60	75	24	33	0

Table 4
Pre-existing crack geometries of flawed specimens with seven different homogeneity indexes (m) (Case III).

Homogeneous index (m)	Flaw angle (α/°)	Ligament angle (β/°)	Flaw length (2a/mm)	Ligament length (2b/mm)	σ_3/MPa
0.6	30	75	24	33	0
1.1					
1.5					
2.0					
3.0					
4.0					
5.0					

Type A   Type B   Type C

(a) Experimental setup (Yang et al. 2008)

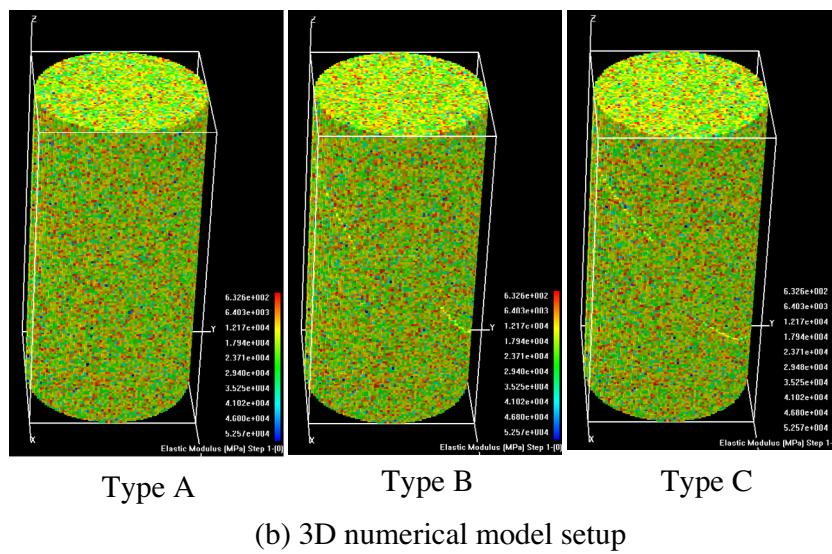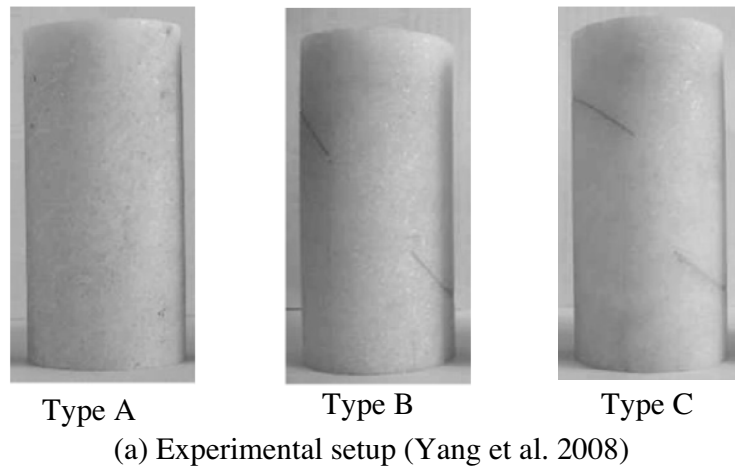Type A   Type B   Type C

(b) 3D numerical model setup

Fig. 3. Three types of geometries of flaws for (a) experimental samples and (b) numerical models. Type A is an intact specimen; Types B and C are flawed specimens with different pre-existing flaws.
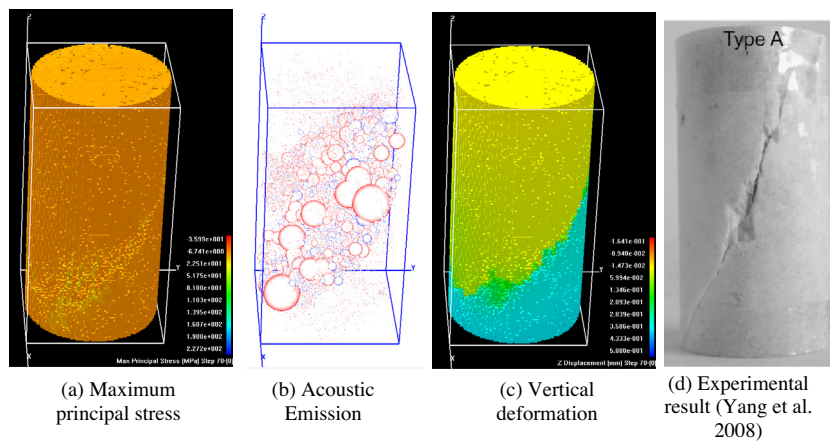

(a) Maximum principal stress   (b) Acoustic Emission   (c) Vertical deformation   (d) Experimental result (Yang et al. 2008)

Fig. 4. 3D numerical predictions for sample at peak stress of stress–strain curve in Fig. 5, compared with experimental results (Type A) (m = 2). (For interpretation of the references to color in this figure legend, the reader is referred to the web version of this article.)
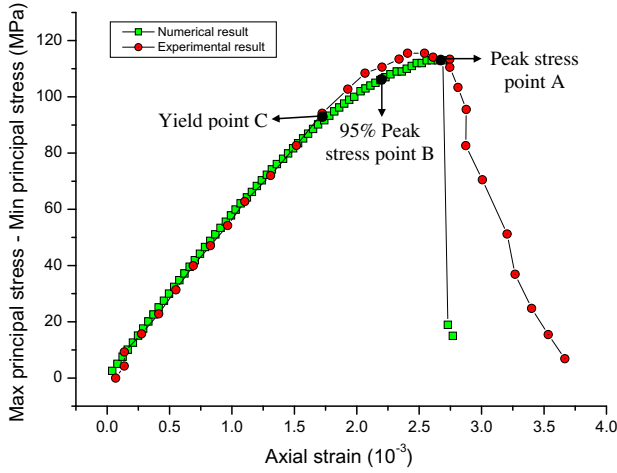
Fig. 5. Stress–strain curves from the experimental test of Yang et al. (2008) and the 3D numerical prediction (uniaxial displacement control) (Type A).

$$D = \begin{cases} 0 & \varepsilon < \varepsilon_{t0} \\ 1 - \frac{\lambda\varepsilon_{t0}}{\varepsilon} & \varepsilon_{t0} \leqslant \varepsilon \leqslant \varepsilon_{tu} \\ 1 & \varepsilon > \varepsilon_{tu} \end{cases} \tag{4}$$

In addition, it is assumed that the damage of mesoscopic elements under multiaxial stress conditions is also isotropic and elastic (Tang, 1997). Under multiaxial stress states, the element can still be damaged in the tensile mode when the equivalent major tensile strain $\bar{\varepsilon}$ exceeds the threshold strain ε_{t0}. The equivalent principal strain $\bar{\varepsilon}$ is defined as (Zhu and Tang, 2006):

$$\bar{\varepsilon} = \sqrt{\langle\varepsilon_1\rangle^2 + \langle\varepsilon_2\rangle^2 + \langle\varepsilon_3\rangle^2} \tag{5}$$

where ε_1, ε_2 and ε_3 are the principal strains and $\langle\ \rangle$ denotes Macaulay's function:

$$\langle x \rangle = \begin{cases} x & x \geqslant 0 \\ 0 & x < 0 \end{cases} \tag{6}$$

The constitutive law for an element subjected to multiaxial stresses can be obtained by substituting the equivalent strain $\bar{\varepsilon}$ for the strain ε in Eqs. (3) and (4). The damage variable then becomes (Wang et al., 2012a,b):

$$D = \begin{cases} 0 & \bar{\varepsilon} < \varepsilon_{t0} \\ 1 - \frac{\lambda\varepsilon_{t0}}{\bar{\varepsilon}} & \varepsilon_{t0} \leqslant \bar{\varepsilon} \leqslant \varepsilon_{tu} \\ 1 & \bar{\varepsilon} > \varepsilon_{tu} \end{cases} \tag{7}$$

In shear failure mode, the damage variable D can be described as follows (Zhu and Tang, 2006):

$$D = \begin{cases} 0 & \bar{\varepsilon} < \varepsilon_{c0} \\ 1 - \frac{\sigma_{rc}}{E_0\bar{\varepsilon}} & \bar{\varepsilon} \geqslant \varepsilon_{c0} \end{cases} \tag{8}$$

where σ_{rc} is the peak strength of the element subjected to uniaxial compression and σ_{c0} is the compressive stress at the point of shear failure.

It is noted that, when considering the effect of the intermediate principal stress, the traditional Mohr–Coulomb strength criterion is not valid (Mogi, 1967). Therefore, in the current study, a simplified unified strength criterion, which is referred to as the twin shear failure criterion, is adopted (Yu, 2004):

$$\begin{aligned} F = \sigma_1 - \frac{\alpha}{2}(\sigma_2 + \sigma_3) = \sigma_t & \quad \sigma_2 \leqslant \frac{\sigma_1 + \alpha\sigma_3}{1+\alpha} \\ F = \frac{1}{2}(\sigma_2 + \sigma_3) - \alpha\sigma_3 = \sigma_t & \quad \sigma_2 > \frac{\sigma_1 + \alpha\sigma_3}{1+\alpha} \end{aligned} \tag{9}$$

where σ_1, σ_2 and σ_3 are the major, intermediate and minor principal stresses, respectively, and α is the influence coefficient of the intermediate principal stress.
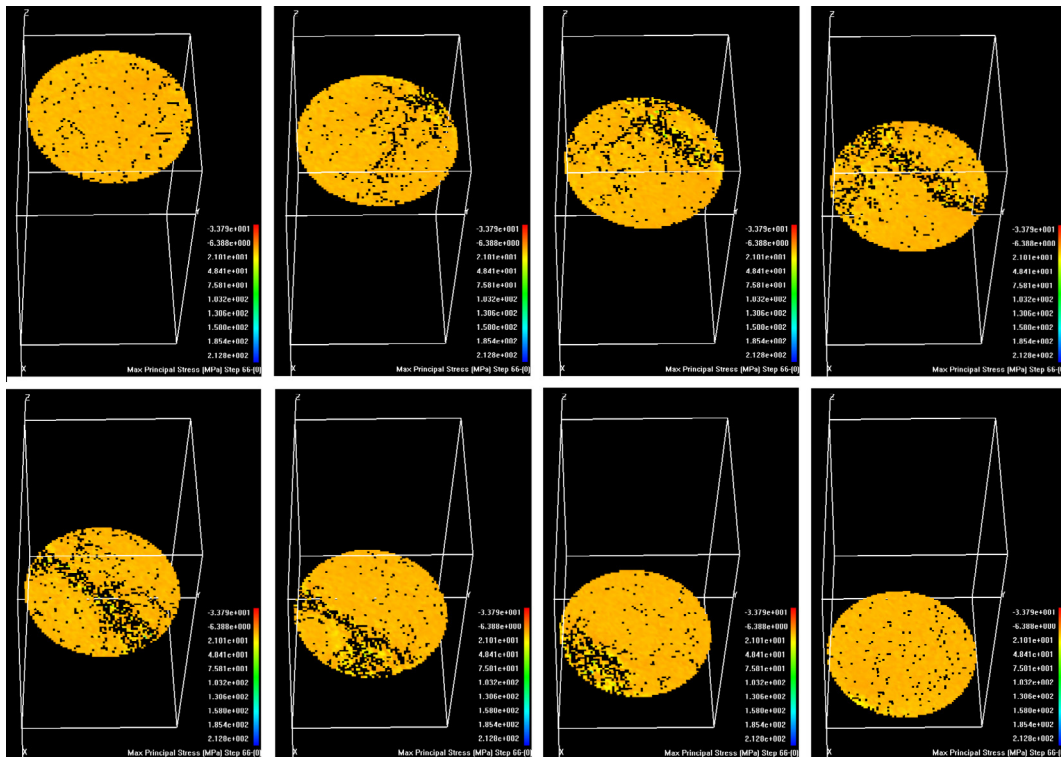

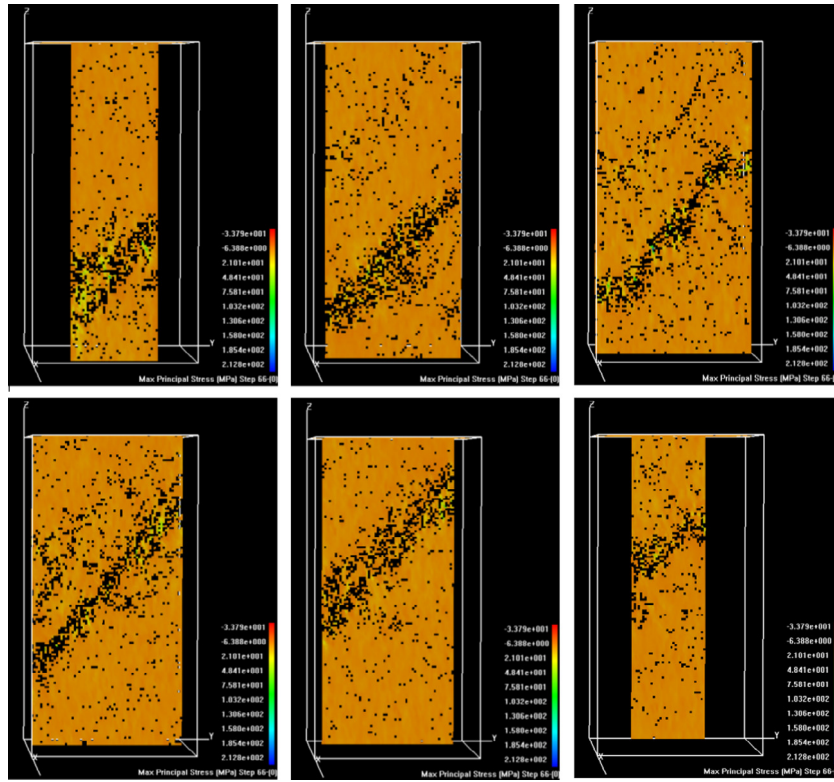**Fig. 6.** Simulated horizontal sections of the specimen at 95% peak stress (Point B in Fig. 5).

Fig. 7. Simulated vertical sections of the specimen at 95% peak stress (Point B in Fig. 5).
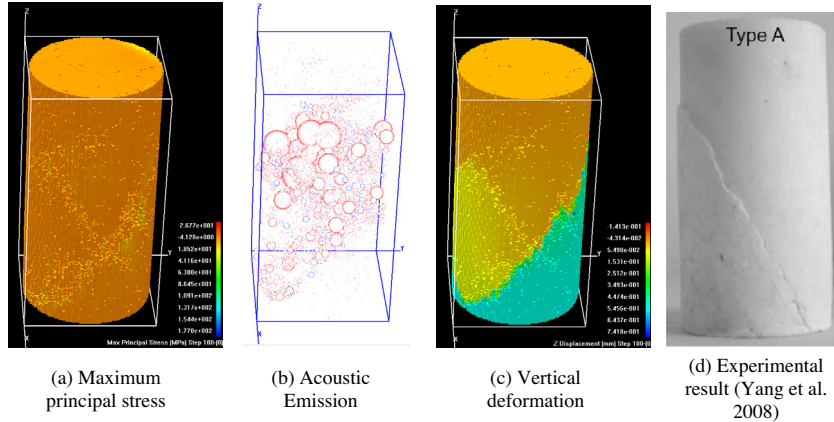

| (a) Maximum principal stress | (b) Acoustic Emission | (c) Vertical deformation | (d) Experimental result (Yang et al. 2008) |

Fig. 8. 3D numerical results for sample (Type A) with confining pressure of 5 MPa and *m* = 2. (For interpretation of the references to color in this figure legend, the reader is referred to the web version of this article.)

In RFPA3D, the failure (or damage) in every element is assumed to be the source of an acoustic event because the failed element must release its elastic energy stored during the deformation. Therefore, by recording the number of damaged elements and the associated amount of energy release, RFPA3D is capable of simulating acoustic emission (AE) activities, including the AE event rate, magnitude and location. The accumulative damage, D can be calculated by the following equation:

$$D = \frac{1}{N} \sum_{i=1}^{s} n_i \qquad (10)$$

where s is the number of calculation steps, n_i is the damaged elements in the *i*th step and N is the total number of elements in

the model. In addition, when the element fails, the energy released is calculated using the relation (Tang et al., 2007).

$$W_i = \frac{1}{2E} (\sigma_1^2 + \sigma_3^2 - 2v\sigma_1\sigma_3) V \qquad (11)$$

where i is the element number, W_i is the released elastic strain energy, E is the elastic modulus, σ_1 and σ_3 are the major and minor principle stresses respectively, v is Poisson's ratio, and V is the element volume (Tang et al., 2007). AE activity indicates the extent of the local damage in the medium, which is directly associated with the evolution and propagation of fractures. By recording the counts of all failed elements and released energies when failure occurs, the AE phenomena associated with the progressive failure process can be simulated.
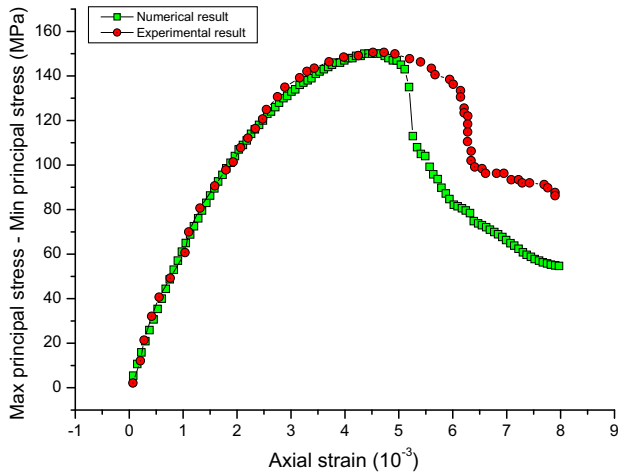
Fig. 9. Stress–strain curves from the experimental test of Yang et al. (2008) and the 3D numerical prediction (confining pressure = 5 Mpa) (Type A).
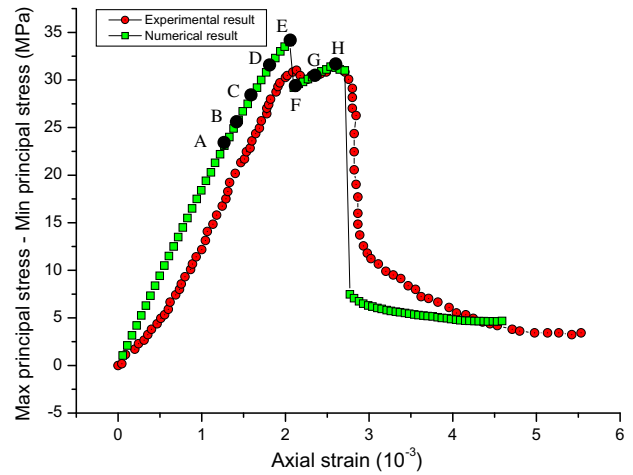

Fig. 11. Stress–strain curves from the experimental test of Yang et al. (2008) and the 3D numerical prediction (uniaxial displacement control) (Type B).

In RFPA3D, the specified displacement (or load) is applied to the specimen incrementally. If some elements are damaged in a particular step, their reduced elastic modulus at each stress or strain level is calculated using the above damage variable D as well as Eq. (2). The calculation is then restarted under the current boundary and loading conditions to redistribute the stresses in the specimen until no new damage occurs. Finally the external load (or displacement) is increased and is used as input for the next step of the analysis. Therefore, the progressive failure process of a brittle material subjected to gradually increasing static loading can be simulated. A user-friendly pre- and post-processor is integrated in RFPA3D to prepare the input data and display the numerical results.

3. Setup of numerical model

Fig. 1 shows the setup of the numerical model. In the numerical model the size of the specimen and the alignment of the two 3-D macroscopic pre-existing flaws are designed to match those in the experimental tests of Yang et al. (2008). Both the uniaxial and conventional triaxial compression experiments for intact and flawed marble samples are simulated numerically. The diameter and height of the specimen is 50 and 100 mm, respectively. In Fig. 1, Fig. 2a is the flaw length; $2b$ is the distance between the tips

of the two internal flaws, which is defined as the ligament length; α is the flaw angle; and β is the ligament angle. To simulate open flaws in rocks, the surfaces of the macroscopic pre-existing flaws are not allowed to overlap. It is further assumed that there is no friction between the two surfaces. Elements within the macroscopic pre-existing flaws are not removed, but replaced by very weak elements with very low elastic moduli (i.e. 10^{-5} MPa) that can be effectively ignored (Liang et al., 2012). The specimens were meshed into $3.14 \times 70^2 \times 140 = 2,160,900$ finite elements. Fig. 2 shows the 3-D hexahedral element distribution in the numerical model. The uniaxial compression strength and elastic modulus of each hexahedral element is assumed to follow the Weibull distribution. A displacement control of 0.002 mm per step was applied axially on the top and bottom of the specimen in order to obtain the total stress–strain response.

In total, three cases are considered. In Case I, in order to evaluate the numerical model against experimental results, three types of flaw geometries are considered. Type A is the case of intact marble without macroscopic pre-existing flaws, whereas Types B and C represent are pre-cracked samples with different flaw geometries. Table 1 describes the pre-existing crack geometries of the flawed specimens. The flaw angles, ligament angles, flaw lengths and ligament lengths are the same as those in the experimental samples tested by Yang et al. (2008). In order to simulate the coarse and
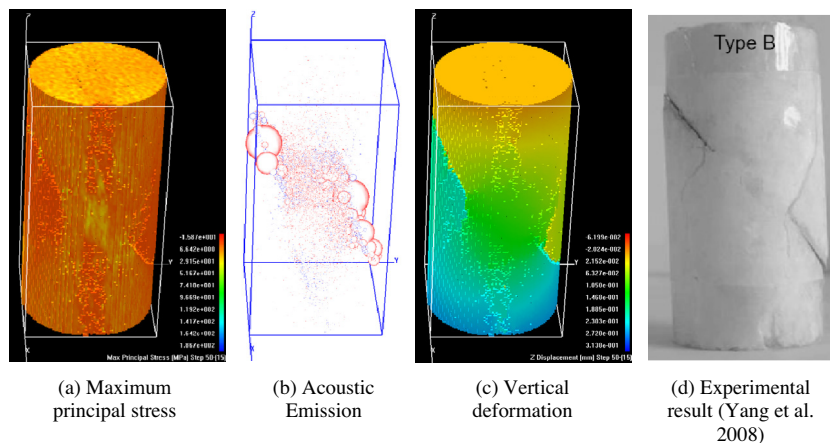

| (a) Maximum principal stress | (b) Acoustic Emission | (c) Vertical deformation | (d) Experimental result (Yang et al. 2008) |

Fig. 10. 3D numerical results for rock specimen (Type B) subjected to uniaxial compression with $m = 1.5$, compared with experimental result. (For interpretation of the references to color in this figure legend, the reader is referred to the web version of this article.)
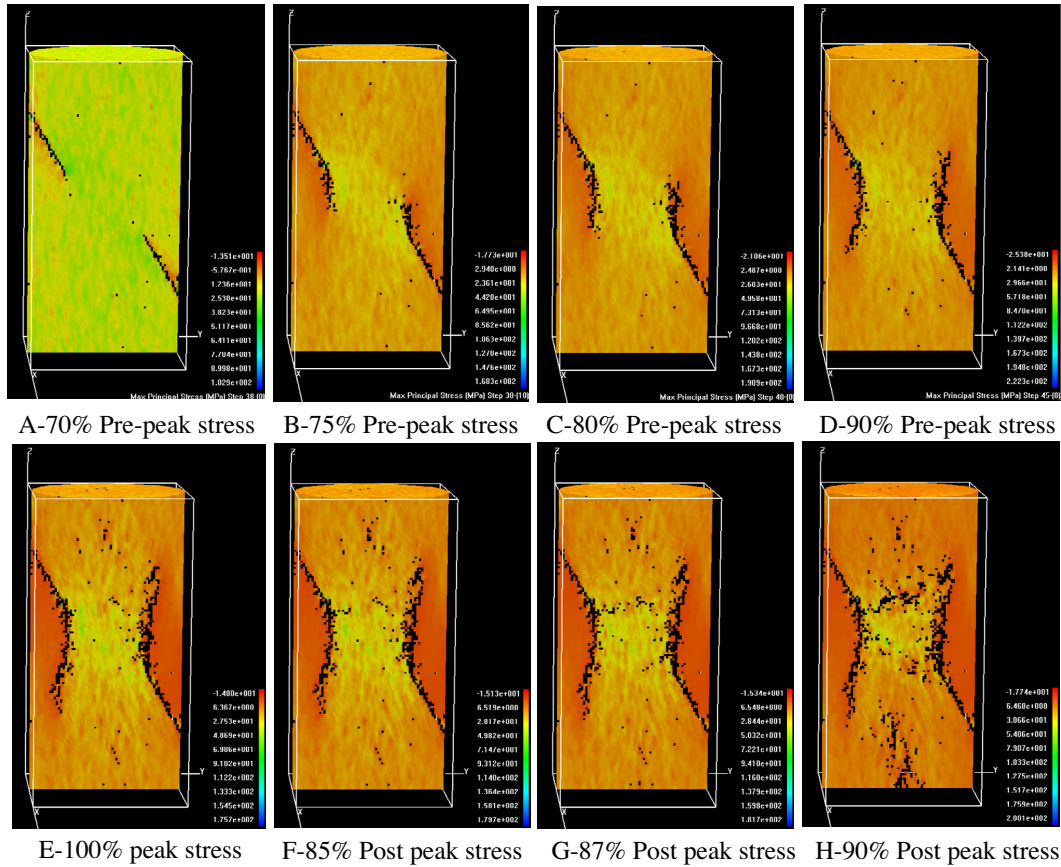
A-70% Pre-peak stress   B-75% Pre-peak stress   C-80% Pre-peak stress   D-90% Pre-peak stress

E-100% peak stress   F-85% Post peak stress   G-87% Post peak stress   H-90% Post peak stress

Fig. 12. Numerically simulated crack evolution in middle vertical slice in Type B specimen.
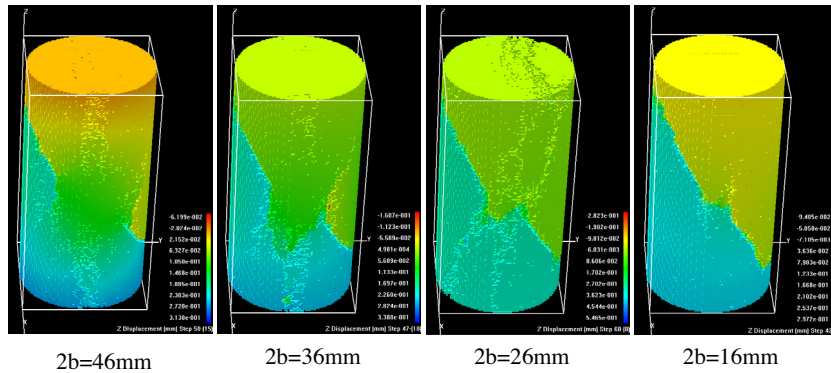

2b=46mm   2b=36mm   2b=26mm   2b=16mm

Fig. 13. Numerically simulated failure modes of specimens with different 2b (Type B).

medium marble in the experimental tests, the homogeneity index (m) is chosen as 1.5 and 2 to describe the coarse and medium marble, respectively. A detailed discussion on the effect of the homogeneous index (m) on the failure modes of the rock specimens will be given in Case III. The initial mean values of the uniaxial compressive strength, elastic modulus and Poisson's ratio for coarse marble were set as 69.83 MPa, 45.54 GPa and 0.25, respectively; and for the medium marble as 119.3 MPa, 49.9 GPa and 0.25, respectively (Yang et al., 2008). The material properties are from this uniaxial compressive simulation and experimental results (Yang et al., 2008). Both the failure pattern and the strength of the numerical specimens and marble specimens used in experiments are more or less the same. Thus, these strength parameters are used in numerical model. It is noted that it is not safe to directly use the macroscopic experimental values as the elemental values in the numerical model. The relationship between them can be seen in Liang et al. (2012).

In Case II, the effect of different ligament angles on the failure modes of the specimen and the total stress–strain response was studied by numerical simulations. In this case, the flaw angle was kept at 30°, while the ligament angles varied as 45°, 60° and 75° (see Table 2). As a comparison, the ligament angle was also kept constant while the flaw angle was changed from 30° to 60° (see Table 3), so as to study the influence of the latter. In Case III, seven different homogeneous indexes (m) are considered. They are 0.6, 1.1, 1.5, 2.0, 3.0, 4.0, 5.0 (see Table 4). According to the Weibull distribution function given in Eq. (1), the higher m values correspond to more homogeneous specimens.
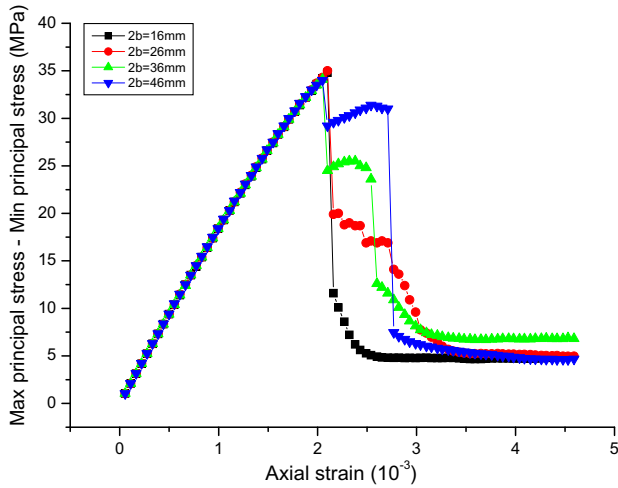
Fig. 14. Numerically simulated axial stress–strain curves specimens with different 2b (Type B).

Fig. 16. Numerically simulated axial stress–strain curves of specimens with different 2b (Type C).

4. Numerical results and discussions

4.1. Experimental evaluation of numerical model (Case I)

In order to validate RFPA3D, the experimental results of Yang et al. (2008) obtained from cylindrical marble samples described in Table 1 are used. Fig. 3 shows the three types of geometries of the (a) experimental samples and (b) numerical models. Type A is an intact specimen, whereas Types B and C contain different macroscopic pre-existing flaws.

4.1.1. Numerical results for rock specimen (Case I-Type A)

Fig. 4 shows the 3-D numerical results of the specimen obtained at the peak stress of the stress–strain curve shown in Fig. 5. Fig. 4(a)–(d) show the maximum principal stress distribution, AE distribution, vertical deformation and the final failure mode of the experimental specimen (Yang et al., 2008), respectively. Comparing Fig. 4(a), (c) and (d), the numerical failure predictions agree well with the experimental results. In particular, the final macro-failure mode is one of shear failure. Fig. 4(b) shows many small red or blue spheres with different diameters. The red spheres represent an AE event due to micro shear damage; the blue ones represent an AE event due to tensile damage; and the diameter of the spheres is proportional to the AE energy released. This plot
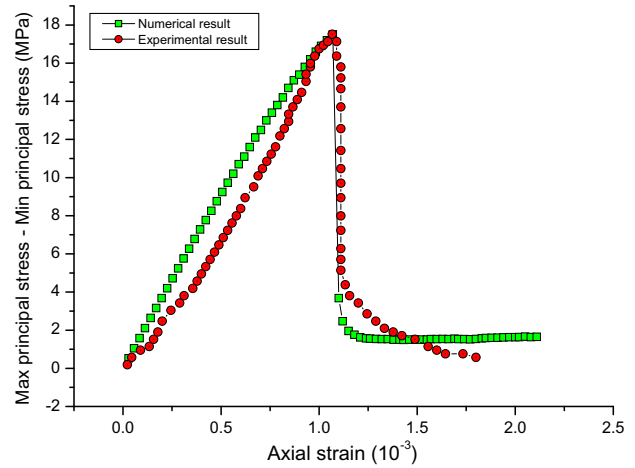
indicates that, under uniaxial compression, both tensile and shear damage occurs, but the latter is dominant in the overall failure process of the specimen.

Fig. 5 compares the numerical and experimental stress–strain curves. The two curves almost overlap before reaching the yield point (Point C). After the yield point, the experimental curve is a little higher than the numerical curve, but the peak stress is almost the same. After the peak point, the numerical curve drops more dramatically than the experimental result. This can be explained by the fact that the homogeneity index (m) of 2 does not completely represent the heterogeneity of the marble in the experimental tests, though the peak stress of the two curves is almost the same. This is also one reason why the predicted final failure mode is not identical to that observed in the experimental tests, though the failure modes are qualitatively the same. As for the effect of m value on the failure modes and the uniaxial compression strength of specimens will be discussed in Section 4.3.

Fig. 4 also shows that, due to the heterogeneity of the rock specimen, the failure modes are not axi-symmetric in either the experimental or numerical results. Experimental tracking of the 3D crack evolution can be obtained using X-ray computer-tomography (CT) (Bésuelle et al., 2000). However, the cost of X-ray CT is still very high. On the other hand, it is straightforward to use the RFPA3D model to estimate the internal micro-damage distribution of the specimen. For example, the horizontal sections of the specimen shown in Fig. 6, and the vertical sections in Fig. 7, indicate the
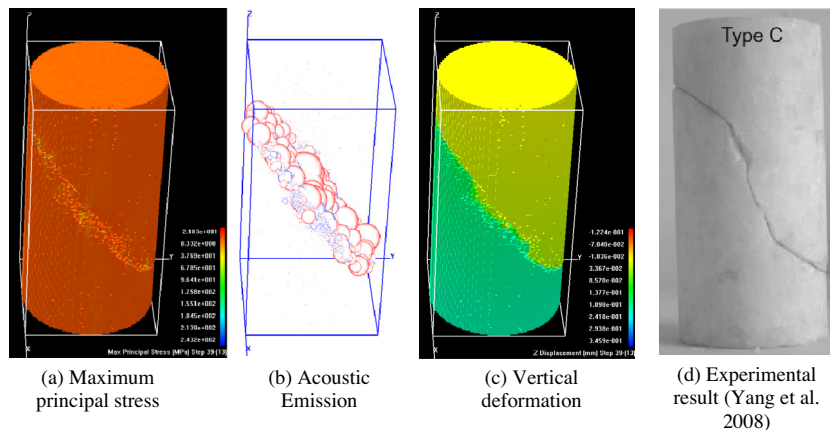

(a) Maximum principal stress   (b) Acoustic Emission   (c) Vertical deformation   (d) Experimental result (Yang et al. 2008)

Fig. 15. 3D numerically simulated results of sample (Type C) subjected to uniaxial compression with m = 1.5, comparing with experimental result. (For interpretation of the references to color in this figure legend, the reader is referred to the web version of this article.)
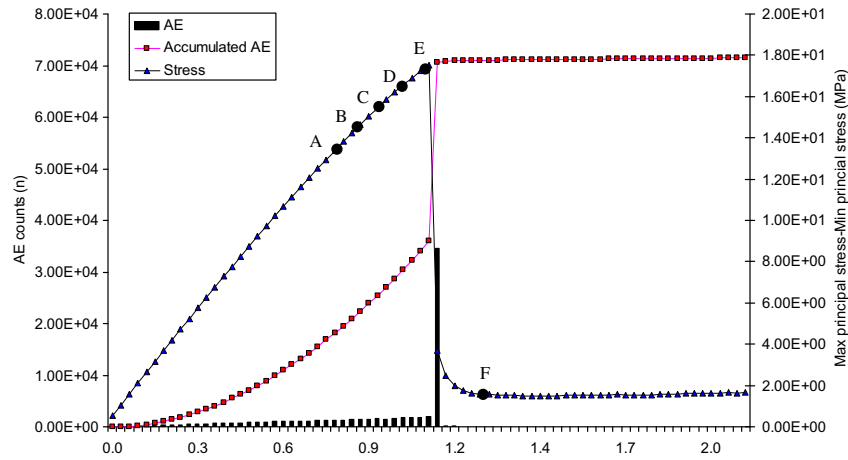
Fig. 17. Numerically simulated axial stress–strain curve and the corresponding acoustic emission (AE) counts for Type C specimen.

A-80% Pre-peak stress   B-85% Pre-peak stress   C-90% Pre-peak stress

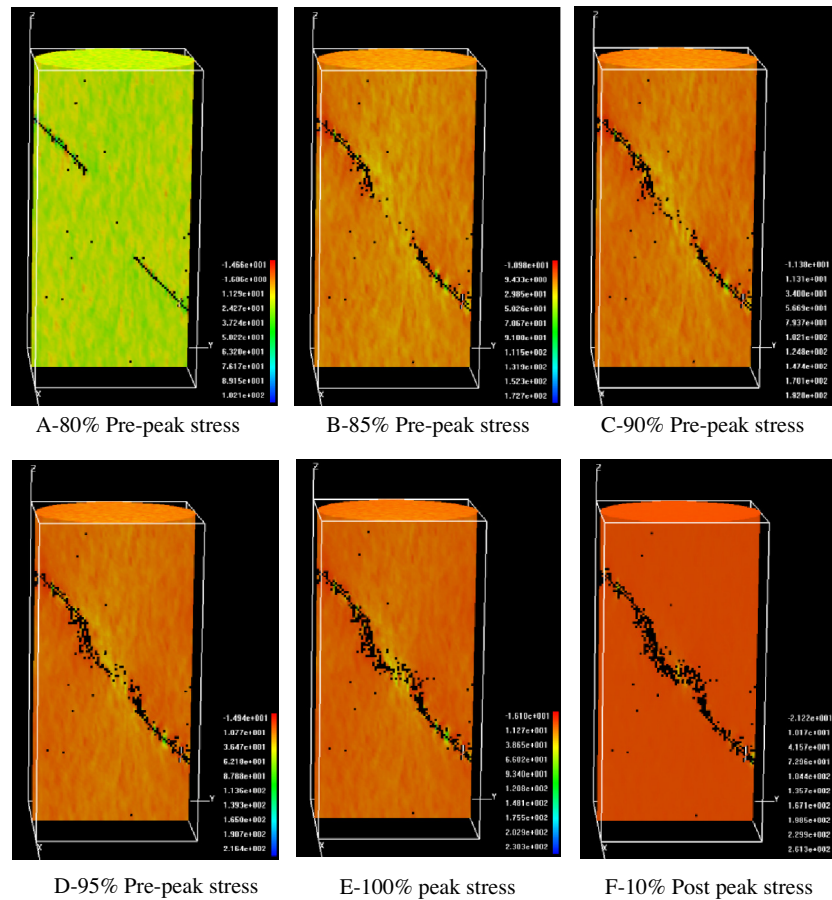D-95% Pre-peak stress   E-100% peak stress   F-10% Post peak stress

Fig. 18. Numerically simulated fracture evolution in middle vertical slice in Type C specimen.

internal micro-damage distributions at 95% peak stress level (Point B in Fig. 5). The micro-damage distribution in Fig. 6 is not axi-symmetric from top to bottom, due to the shear failure mode. Likewise, in Fig. 7, the micro-damage distribution is not axi-symmetric from front to back, due to the heterogeneity of the rock specimen.

Fig. 8 presents the numerical failure modes of the specimen with a confining pressure of 5 MPa. Due to the effect of the latter, the macro-shear failure mode is more pronounced, though another less distinct shear crack is oriented about 80–90° (normal) to the main shear crack (see Fig. 8(a) and (c)). Although the secondary

shear crack was not observed from the surface of the marble in the experimental tests (Fig. 8(d)), the dominant macro-shear crack is quantitatively the same as the numerically simulated one. Fig. 8(b) shows the AE distribution. This plot indicates that the shear damage (marked by red spheres) again dominates, because the confining pressure restrains the growth of the tensile damage. The numerical and experimental stress–strain curves, shown in Fig. 9, almost overlap before the peak stress is reached. The post-peak curves for this case show a pronounced softening, unlike the brittle behaviour for the uniaxial compression sample in

Fig. 5. This phenomenon from brittle to ductile transition was discussed by Rutter (1986) in details. As expected, due to the confining pressure, the peak stress in Fig. 9 is much higher than that for the case of uniaxial compression (Fig. 5). It is noted that the numerically simulated post-peak stress softening so rapidly as compared to the experimental values is likely due to the input residual strength coefficients (λ) in Eq. (3). As there are no corresponding residual strength coefficients in Yang et al. (2008), the current input value of λ is 0.3, which is likely lower than the real residual strength coefficient. In addition, the softening of post-peak stress is also affected by the confining pressure and the heterogeneity of material, which can be seen in Wang et al. (2012b).

4.1.2. Numerical results for rock specimen (Case I-Type B)

For Type B, the flaw length (2a) and ligament length (2b) are 24 and 33 mm, respectively. The flaw angle (α) and ligament angle (β) are 30° and 38°, respectively. Fig. 10(a)–(c) show the numerical

results for the rock specimen with macroscopic pre-existing flaws (Type B). Fig. 10(d) is the corresponding experimental result. Fig. 10(c) shows that the wing (tensile) cracks grow almost normally to the macroscopic pre-existing flaws. From the surface of the specimen, it appears that the shear cracks between the two macroscopic pre-existing flaws do not occur. Accordingly, it seems no macroscopic crack coalescence is observed during the whole failure process. Fig. 10(b) shows the AE distribution, where the shear damage (represented by red spheres) dominates with only a modest amount of tensile damage (small blue spheres) along the macroscopic pre-existing flaws. In Fig. 11, the numerical stress–strain curve is very similar to the experimental one. It is noted that from these two curves, two slightly different peak stresses are observed.

Fig. 12 shows the simulated internal crack evolution in the middle cross-section of the specimen. The selected figures are related to the points indicated in the stress–strain curve in Fig. 11. From
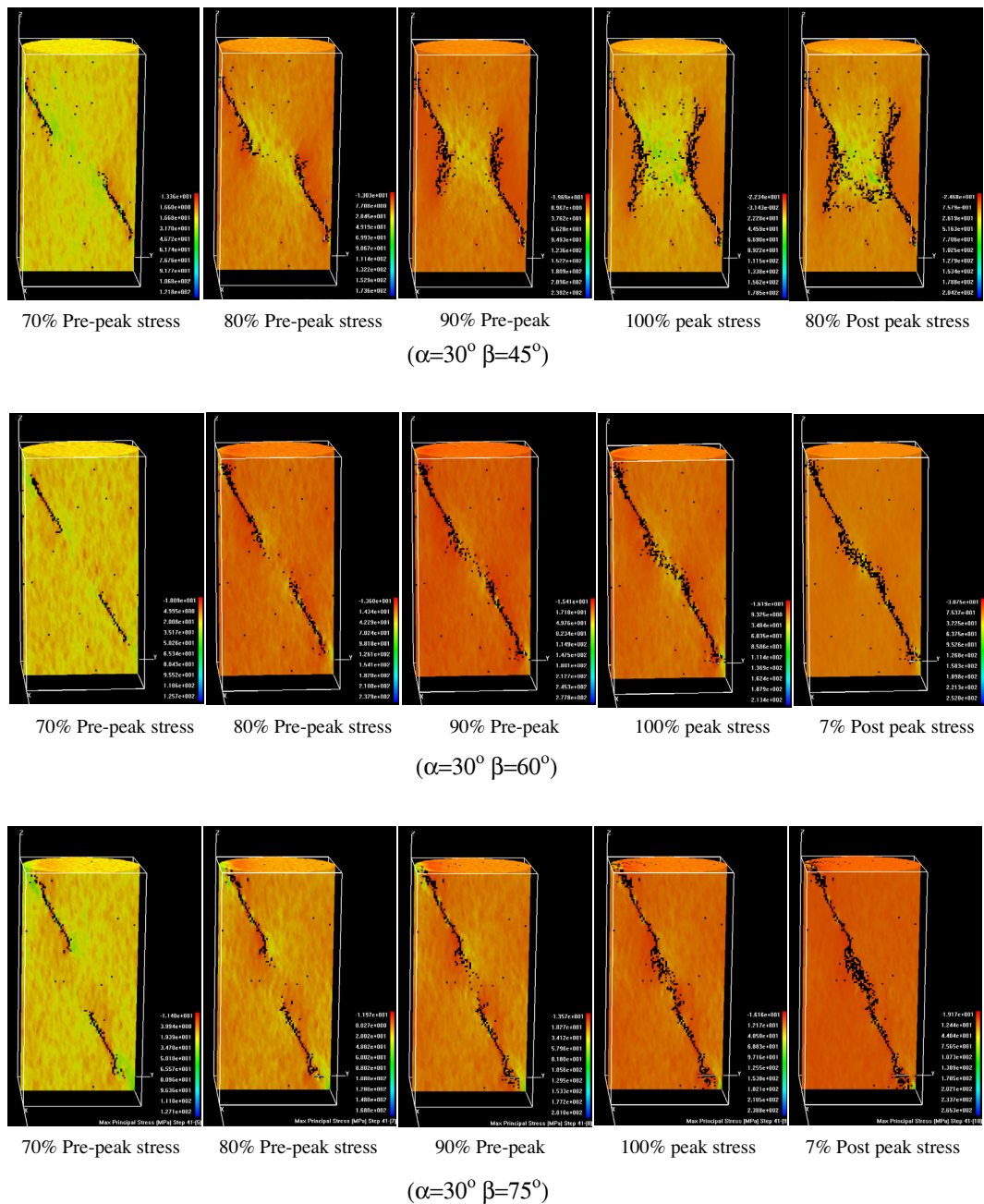

| 70% Pre-peak stress | 80% Pre-peak stress | 90% Pre-peak | 100% peak stress | 80% Post peak stress |

(α=30° β=45°)

| 70% Pre-peak stress | 80% Pre-peak stress | 90% Pre-peak | 100% peak stress | 7% Post peak stress |

(α=30° β=60°)

| 70% Pre-peak stress | 80% Pre-peak stress | 90% Pre-peak | 100% peak stress | 7% Post peak stress |

(α=30° β=75°)

Fig. 19. Numerically simulated the effect of ligament angle (β) on the fractures evolutions from two pre-existing flaws (uniaxial loading).
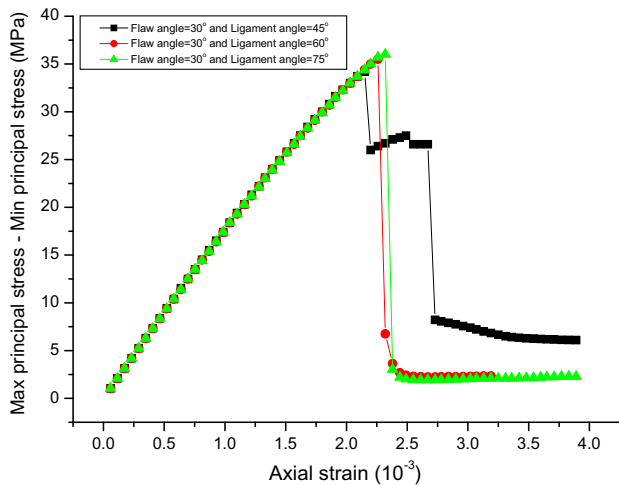
Fig. 20. Numerically simulated axial stress–strain curves of specimens with the same flaw angle but different ligament angles (uniaxial loading).

Fig. 12, with the increase in uniaxial loading, some damaged elements are observed near the macroscopic pre-existing flaws when the stress level is about 70% of the peak stress. When the stress reaches 75% of its peak value, the wing cracks grow from the internal ends of the two macroscopic pre-existing flaws. Subsequently, the two wing cracks continue to propagate when the stress level is at the peak stress (Point E in Fig. 11). After the peak stress is reached, there is a distinct stress drop to 85% of the post peak stress (Point F). At this time, new cracks initiate from the two ends of the two macroscopic pre-existing flaws, and propagate to the other flaw and coalesce when the stress level reaches the 90% of the post peak stress (Point H). In Fig. 11, the stress–strain curve increases again to Point H. Comparing Fig. 10c and Fig. 12, the actual internal crack evolution in the latter is very different to the surface cracking observed in the former, where no crack interaction can be observed.

In order to evaluate whether the ligament length (2b) affects the coalescence of the cracks from the two internal ends of the macroscopic pre-existing flaws, four numerical tests for the specimens with different ligament lengths (2b) of 16, 26, 36, and 46 mm were performed. The numerically simulated failure modes for the specimens, shown in Fig. 13, indicate that with a decrease in the ligament length (2b) the coalescence of the surface cracks can be observed clearly. When 2b is set to 16 mm, the growth of the wing (tensile) cracks is restrained, but the shear cracks between the macroscopic pre-existing flaws propagate and then coalescence. The axial stress–strain curves of the four numerical tests, shown in Fig. 14, indicate that the first peak stresses for the four cases are almost the same. However, with the ligament length is decreased, the second peak stresses also decrease. Indeed, when 2b is 26 mm there is not obvious second peak stress, whereas when 2b is 16 mm there is no peak stress at all. As discussed in Fig. 12, the second peak stress actually represents the further loading needed to cause the cracks between the macroscopic pre-existing flaws to coalesce. For the case of 2b equal to 16 mm, the short ligament length enables the cracks to coalesce easily from the two ends of the macroscopic pre-existing flaws.

4.1.3. Numerical results for rock specimen (Case I-Type C)

For the Type C tests, the flaw length (2a) and ligament length (2b) is 24 and 33, respectively, while the flaw angle (α) and the ligament angle (β) is fixed at 45° and 61°. Compared with the Type B cases, the flaw length and the ligament length are the same, but the flaw angle and ligament angle are different. From Fig. 15(a) and (c),

the numerically simulated shear failure mode is in good agreement with the experimental observations give in Fig. 15(d). In this case, almost no wing cracks are observed; only shear cracks grow from the two ends of the macroscopic pre-existing flaws and then coalescence. However, from the AE distribution of Fig. 15b, both shear damage (red spheres) and tensile damage (blue spheres) are observed. This indicates that macro-shear failure can be formed by both micro-tensile and shear damage, but the latter dominates. In addition, Fig. 16 shows that the numerically simulated axial stress–strain curve is in agreement with the experimental results of Yang et al. (2008).

Fig. 17 shows the numerically simulated axial stress–strain curve, as well as the corresponding AE and accumulated AE counts. Fig. 18 shows the numerically simulated evolution of the internal cracks in the middle slice of the specimen. The selected figures are related to the points in the stress–strain curve of the numerical simulations in Fig. 17. From this Figure, with an increase in the applied uniaxial loading, the stress increases almost linearly with the axial strain prior to reaching the peak stress at point E. Simultaneously, the AE counts increase gradually up to the peak stress point, where a distinct stress drop occurs and there is sudden surge in the AE counts. From Fig. 18, it is evident that the internal cracks in the middle slice of the specimen firstly grow along the axis of the vertical compression stress, from Point A to Point B. When the stress level reaches 90% of the peak value (Point C), shear cracks start to grow and damage a rock bridge (Wong and Chau, 1998) in stages D and E. In stage F, the shear cracks coalescence.

4.2. Numerical simulations of the effect of the flaw angle and ligament angle on the failure modes and uniaxial compression strength (Case II)

In the experimental tests conducted by Yang et al. (2008), the effect of the flaw angle and the ligament angle on the final failure mode and the uniaxial compression strength was not considered. These issues will now be investigated numerically using RFPA3D.

Fig. 19 shows the numerically simulated crack evolutions from the macroscopic pre-existing flaws with the same flaw angle but different ligament angle. When α is 30° and β is 45°, cracks initiate as wing cracks and propagate gradually along the direction of the vertical compression stress. After the peak stress is passed, some shear cracks grow and coalesce. When the ligament angle (β) increases to 60°, no wing cracks are observed, but the shear cracks grow from the two ends of the macroscopic pre-existing flaws and coalescence finally at the peak stress. For a further increase of the ligament angle to 75°, the macroscopic pre-existing flaws are in the same line and the shear cracks initiate, propagate and coalescence. Thus the two macroscopic pre-existing flaws are connected by shear cracks between them. Fig. 20 illustrates the three numerically-simulated axial stress–strain curves. The peak stress shows a moderate increase as the ligament angle increases from 45° to 75°. This indicates that wing tensile cracks dominate for a ligament angle of 45°, and lower the uniaxial compression strength. As a comparison, the ligament angles of 60° and 75° cause a failure mode which is dominated by shear cracks, resulting in higher uniaxial compression strengths.

Fig. 20 shows the numerically simulated crack evolutions from the macroscopic pre-existing flaws with the same ligament angle but different flaw angles. Fig. 21 suggest that when the ligament angle (β) is 75° and the flaw angle (α) is 30° or 45°, wing cracks do not occur, but shear cracks grow from the two ends of the macroscopic pre-existing flaws and eventually coalescence. For the case of a flaw angle of 60°, the cracks do not initiate the ends of the flaw, but from the middle, and then propagate to the flaw below. Finally, a shear band forms and connects the macroscopic pre-existing flaws. The numerically simulated axial stress–strain curves, plotted in Fig. 22, show that the peak stress is the lowest

for a flaw angle of 45° and highest for a flaw angle of 60°. These numerical results are in broad agreement with the other experimental and numerical findings (Tien et al., 2006; Wang et al., 2012b).

4.3. Numerical simulations of the effect of heterogeneity on the failure modes and uniaxial compression strength (Case III)

As indicated previously, it is difficult to control the heterogeneity of a cylindrical marble specimen in laboratory testing, with only the simple description of "coarse" and "medium" being adopted (see Fig. 23). In this section, to study the effect of the heterogeneity on the failure mechanism, different homogeneity indexes of 0.6, 1.1, 1.5, 2.0, 3.0, 4.0 and 5.0 were selected. For each of these cases, the final stage of failure of the specimen (Fig. 24), plots of the axial stress–strain response (Fig. 27), and the corresponding AE/Accumulated AE counts (Fig. 28) are examined under uniaxial compression.

In Fig. 24, for the heterogeneous rock (e.g. m = 0.6 or 1.1), many micro-cracks are distributed around the main cracks. Fig. 25 shows the crack evolutions and corresponding AE distribution for the middle slice of the rock specimen. From this Figure, it appears that micro-cracks occur not only near the macroscopic pre-existing flaws, but also randomly throughout the whole specimen prior to reaching 60% of the peak stress level. As the uniaxial compression is increased, the micro-cracks start to cluster around the main shear cracks between the two macroscopic pre-existing flaws. When the stress level reaches its peak, the main shear cracks coalescence to form a shear band connecting the macroscopic pre-existing flaws. It appears that both tensile cracks (red spheres) and shear cracks (blue spheres) contribute to the final failure of the rock specimen, and are observed in the AE distribution plots. For the stress–strain plots with m = 0.6 and 1.1, shown in Fig. 27, the yield points occur at a relatively low stress level, and the post-peak curves show obvious plastic behaviour. However, for the relatively homogeneous rock (e.g. m = 1.5 and 2.0), the number of micro-cracks around the
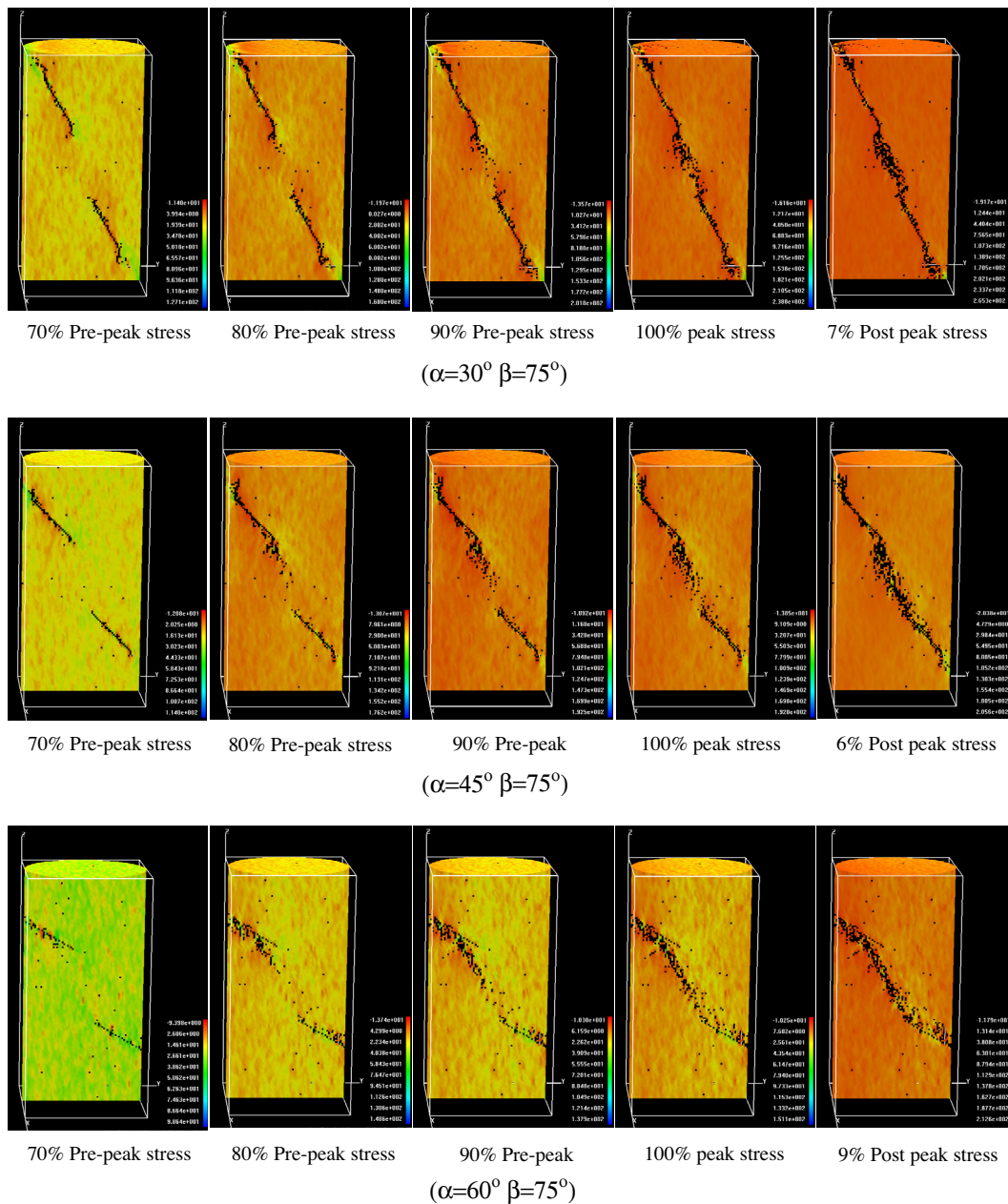

| 70% Pre-peak stress | 80% Pre-peak stress | 90% Pre-peak stress | 100% peak stress | 7% Post peak stress |

(α=30° β=75°)

| 70% Pre-peak stress | 80% Pre-peak stress | 90% Pre-peak | 100% peak stress | 6% Post peak stress |

(α=45° β=75°)

| 70% Pre-peak stress | 80% Pre-peak stress | 90% Pre-peak | 100% peak stress | 9% Post peak stress |

(α=60° β=75°)

Fig. 21. Numerically simulated the effect of flaw angle (α) on the fractures evolutions from two pre-existing flaws.
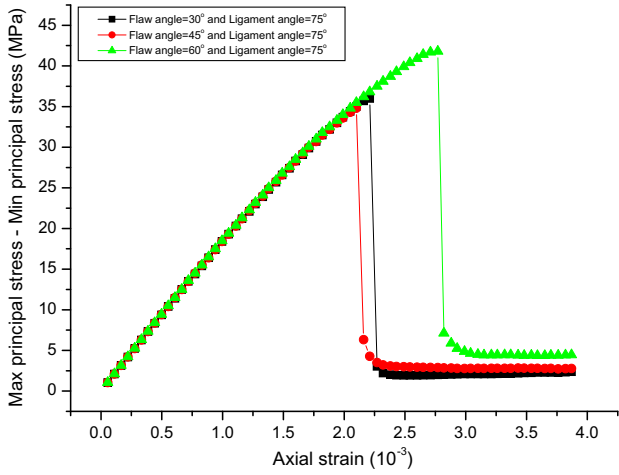
Fig. 22. Numerically simulated axial stress–strain curves of specimens with the same ligament angle but different flaw angles.

main shear cracks between the macroscopic pre-existing flaws is reduced (see Fig. 24). Comparing with the cases which have lower m values of 0.6 and 1.1, the yield point rises, but the post-peak curves show a distinct brittle behaviour. Indeed, the stress–strain plots display a sharp drop after passing the peak stress.

For the highly homogeneous rock (e.g. m = 3, 4 and 5), the number of micro-cracks developed is much lower and more concentrated. For example, Fig. 26 shows the crack evolutions and the corresponding AE distribution for the middle slice of the rock specimen. At a stress level equal to 85% of the peak value, only a few micro-cracks are concentrated the macroscopic pre-existing flaws, which is indicated by the fewer and smaller red/blue spheres in the corresponding AE distribution plot. When the stress levels reaches 90% of the peak stress, the main shear cracks initiate and propagate from the two ends of the macroscopic pre-existing flaws. No micro-cracks around the main shear cracks are observed, which is very different from the cases with lower m values of 0.6 and 1.1. This also can be confirmed from the corresponding AE distribution plot, where no red/blue spheres are found around the shear band.
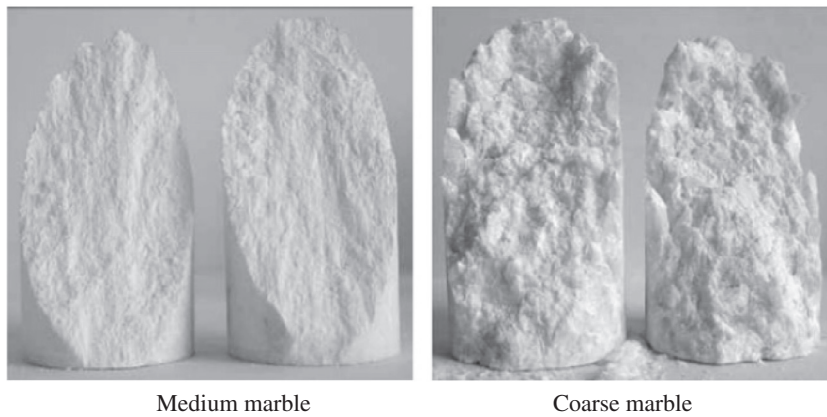

Medium marble Coarse marble

Fig. 23. Experimental results of failure of medium and coarse marble specimens (Yang et al., 2008).

m=0.6 m=1.1 m=1.5 m=2.0
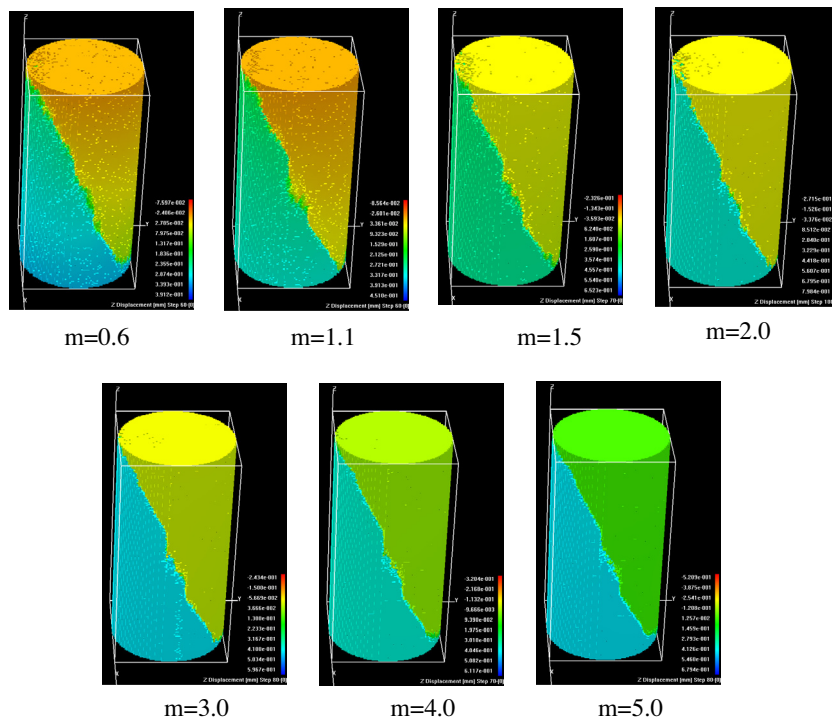
m=3.0 m=4.0 m=5.0

Fig. 24. Numerically simulated failure mode of specimens with different homogeneous index (m) of 0.6, 1.1, 1.5, 2.0, 3.0, 4.0 and 5.0, respectively (α = 30° β = 75°).

| 60% Pre-peak stress | 75% Pre-peak stress | 90% Pre-peak stress | 100% peak stress | 70% Post peak stress |

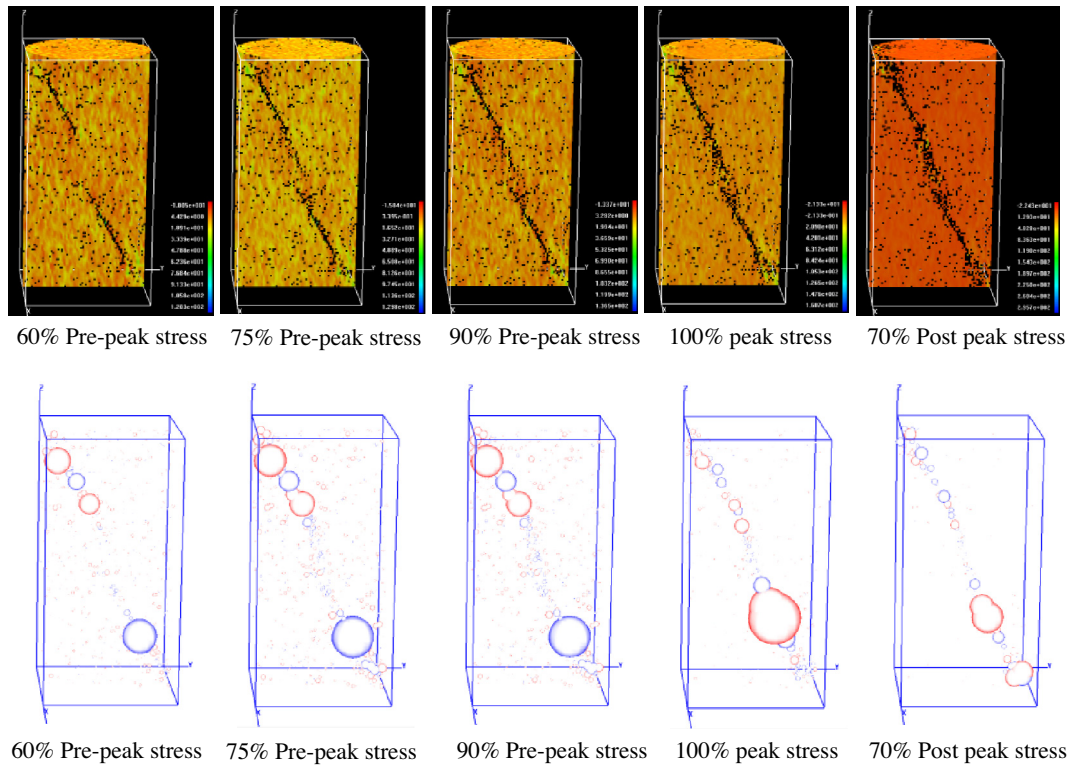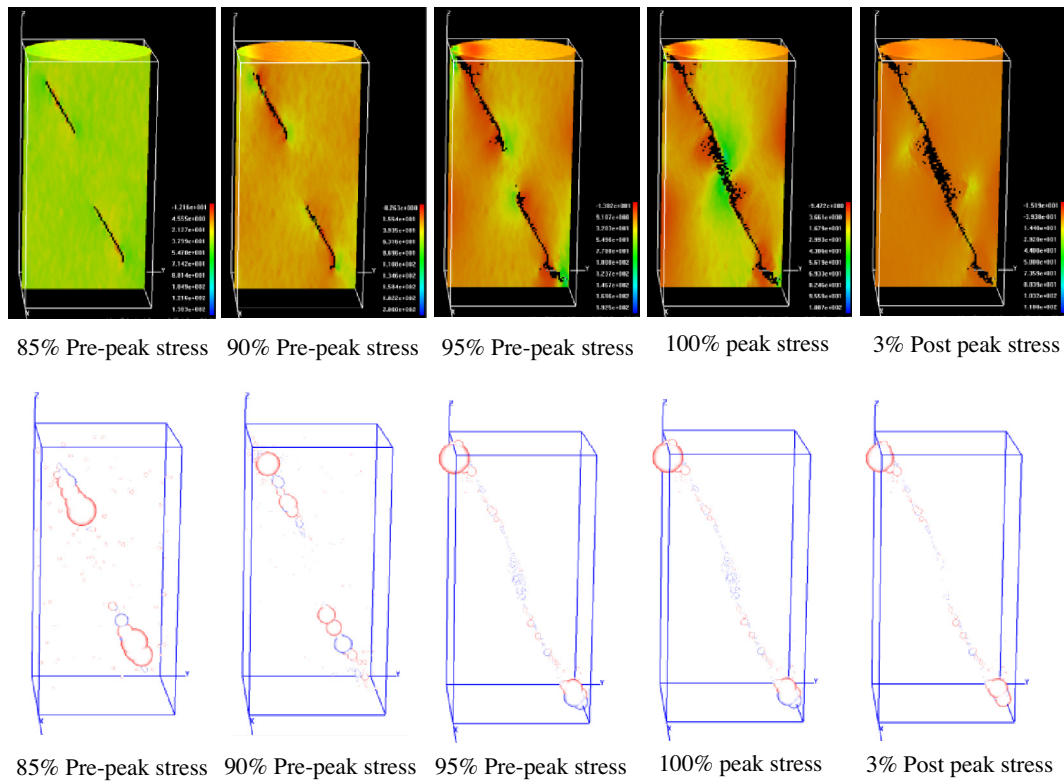| 60% Pre-peak stress | 75% Pre-peak stress | 90% Pre-peak stress | 100% peak stress | 70% Post peak stress |

Fig. 25. Numerically simulated fractures evolution and the corresponding AE distribution from two pre-existing flaws in a cylindrical specimen ($m = 0.6$) ($\alpha = 30°$ $\beta = 75°$). (For interpretation of the references to color in this figure legend, the reader is referred to the web version of this article.)

| 85% Pre-peak stress | 90% Pre-peak stress | 95% Pre-peak stress | 100% peak stress | 3% Post peak stress |

| 85% Pre-peak stress | 90% Pre-peak stress | 95% Pre-peak stress | 100% peak stress | 3% Post peak stress |

Fig. 26. Numerically simulated fractures evolution and the corresponding AE distribution from two pre-existing flaws in a cylindrical specimen ($m = 5.0$) ($\alpha = 30°$ $\beta = 75°$). (For interpretation of the references to color in this figure legend, the reader is referred to the web version of this article.)
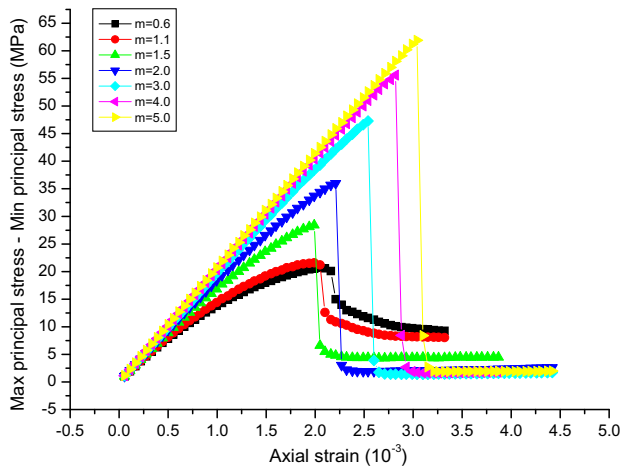
Fig. 27. Numerically simulated axial stress–strain curves of specimens with different homogeneity index (m) of 0.6, 1.1, 1.5, 2.0, 3.0, 4.0 and 5.0, respectively ($\alpha = 30° \; \beta = 75°$).
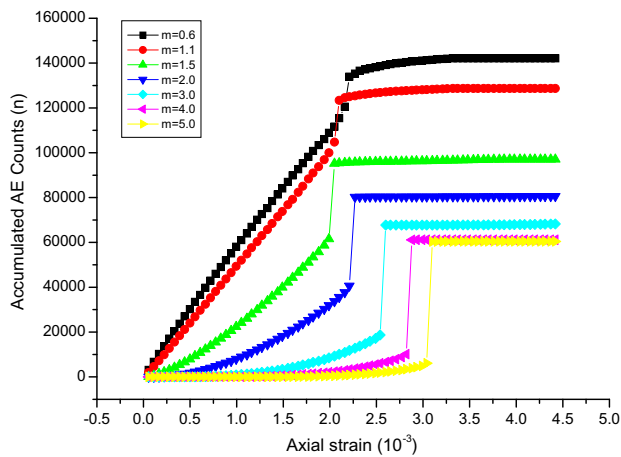

Fig. 28. Numerically simulated accumulated AE of specimens with different homogeneity index (m) of 0.6, 1.1, 1.5, 2.0, 3.0, 4.0 and 5.0, respectively ($\alpha = 30° \; \beta = 75°$).

Various numerically-simulated axial stress–strain curves are shown in Fig. 27. These show that the relatively heterogeneous rocks (e.g. $m = 0.6$ or 1.1) have a gentler post-peak behaviour. For increasingly homogeneous rocks with higher m (e.g. $m = 1.5$, 2, 3, 4, or 5), the behaviour becomes increasingly brittle and the peak stress (or strength) of the specimens increases. As a result, the curve becomes more linear and the post-peak loss in strength is also more precipitous. Clearly, the axial stress–strain curves depend strongly on the heterogeneity of the specimens. This can be explained by noting that, with an increase in m, the Weibull distribution (Eq. (1)) dictates that the Young's modulus and uniaxial compression strengths of more of the elements will be clustered around x_0. Thus, more elements with a high Young's modulus and uniaxial compression strength will be distributed in the rock mass, and higher applied loads will be needed to cause damage to such elements. This is the reason why the peak stress increases dramatically with m in Fig. 27.

Finally, Fig. 28 shows the cumulative number of AE events when the homogeneity index (m) increases from 0.6 to 5. According to the Weibull distribution in Eq. (1), a larger value of m implies a more homogeneous material and vice versa. Under the same loading and boundary conditions, fewer damaged elements will occur in the more homogeneous material. This is confirmed in Fig. 28,

where the cumulative number of AE events decreases as m increases. For instance, when $m = 0.6$ and 1.1, the final cumulative number of AE events is 142,109 and 128,703, respectively. When m is 3, 4 and 5, the final cumulative number of AE events is 68216, 61161 and 60405, respectively.

5. Conclusions and discussions

A three-dimensional numerical model (RFPA3D) was introduced to investigate the failure process and uniaxial compression strength of cylindrical rock specimens with two macroscopic pre-existing flaws. The main feature of RFPA3D is that it can simulate the evolution of cracks in three-dimensional space, which is much more complex than the two-dimensional crack regimes that commonly studied. Tensile or shear cracks were simulated when certain local stress conditions were exceeded. Another unique feature of this model is that no *priori* assumptions are necessary about where and how cracks occur. Moreover, the model is able to capture the heterogeneity of rock specimens using a probabilistic variation of its mechanical properties.

Numerical results show that, for an intact specimen under uniaxial compression, both tensile and shear damage occurs. In general, shear damage dominates the failure process because the confining pressure restrains the growth of tensile damage. The simulated failure mode and uniaxial compression strength are in agreement with the experimental results reported by Yang et al. (2008). The numerical simulations are able to model the evolution of internal cracks inside the rock specimen. Due to the effects of heterogeneity, the micro-damage distributions are not axi-symmetric from top-to-bottom and from front-to-back.

For specimens with macroscopic pre-existing flaws, the simulated surface failure modes and uniaxial compression strength also agree with the experimental results. Moreover, the internal crack evolution process was simulated successfully. Although the coalescence of the cracks between macroscopic pre-existing flaws cannot be easily observed in laboratory testing, they can be predicted by numerical modelling. The effect of the ligament length on the coalescence of cracks was investigated numerically, and the predictions agreed well with experimental tests of Yang et al. (2008).

In addition, the numerical results show that both the flaw angle and the ligament length can affect the final failure modes and the uniaxial compression strength of the rock specimen. The uniaxial compression strength increases slightly with increasing ligament angle. The uniaxial compression strength is the lowest when the flaw angle equals 45°. These numerical results are in agreement with the corresponding experimental results reported by Tien et al. (2006) and Wang et al. (2012b).

The numerical results also show that the higher the homogeneity index (m), the higher the strength of the specimen is. As m increases, the stress–strain curve becomes more linear and the post-peak loss strength is also more precipitous. During the failure process of specimens, the cumulative number of acoustic emission events increases with increasing m values.

It is noted that the initiation and propagation of flaws in 3D space are affected by many factors, such as flaw orientation, flaw thickness, flaw depth, the friction and sliding on slip surfaces of the flaws, the heterogeneity of material and loading style. The numerically simulated failure modes do not appear always to compare very convincingly with the experimental depiction of these as presented in the paper. Therefore, this numerical model needs further experimental and theoretical analysis. For example, the input homogeneous index (m) in the numerical model will be further validated quantitatively by experimental tests. Furthermore, in the RFPA simulation, the mesh dependency is unavoidable, which has been detailed in previous publications. However, if the rock

specimen is simulated with the relatively small element size, the mesh dependency is ignorable to some degree. Under this small size of elements, the mesh dependency may affect the quantity of the numerical results. We just use an optimal element size here to address the crack issues here, while the numerical issues related with element size and its effects will be addressed in an alternative paper. Nevertheless, the numerical results demonstrate many phenomena that have already been shown in laboratory experiments. This study highlights some interesting phenomena for improving the understanding of the mechanism of 3D rock fracturing.

Acknowledgments

References

Amitrano, D., Helmstetter, A., 2006. Brittle creep, damage, and time to failure in rocks. J. Geophys. Res. 111 (B11201), 1–17.

Ashby, M.F., Hallam, S.D., 1986. The failure of brittle solids containing small cracks under compressive stress states. Acta Metall. 34, 497–510.

Bésuelle, P., Desrues, J., Raynaud, S., 2000. Experimental characterisation of the localisation phenomenon inside a Vosges sandstone in a triaxial cell. Int. J. Rock Min. Sci. 37, 1223–1237.

Blair, S.C., Cook, N.G.W., 1998. Analysis of compressive fracture in rock using statistical techniques: Part I. A non-linear rule-based model. Int. J. Rock Mech. Min. Sci. 35 (7), 837–848.

Bobet, A., 1997. Fracture coalescence in rock materials: experimental observations and numerical predictions. Sc.D. thesis, MIT, Cambridge, USA.

Bobet, A., 2000. The initiation of secondary cracks in compression. Eng. Fract. Mech. 66, 187–219.

Bobet, A., Einstein, H.H., 1998. Fracture coalescence in rock-type materials under uniaxial and biaxial compression. Int. J. Rock Min. Sci. 35, 863–889.

Brace, W.F., Bombolakis, E.G., 1963. A note on brittle crack growth in compression. J. Geophys. Res. 68 (12), 3709–3713.

Brantut, N., Heap, M.J., Meredith, P.G., Baud, P., 2013. Time-dependent cracking and brittle creep in crustal rocks: a review. J. Struct. Geol. 52, 17–43.

Fanella, D., Krajcinovic, D., 1988. A micromechanical model for concrete in compression. Eng. Fract. Mech. 29, 49–66.

Feng, X.T., Pan, P.Z., Zhou, H., 2006. Simulation of the rock microfracturing process under uniaxial compression using an elasto-plastic cellular automaton. Int. J. Rock Mech. Min. Sci. 43 (7), 1091–1108.

Germanovich, L.N., Salganik, R.L., Dyskin, A.V., Lee, K.K., 1994. Mechanisms of brittle fracture of rock with pre-existing cracks in compression. Pageoph 143 (1/2/3), 117–149.

Griffith, A.A., 1924. The theory of rupture. In: Proc. 1st Int. Congr. on Applied Mech., Delft, pp. 55–63.

Healy, D., Jones, R.R., Holdsworth, R.E., 2006a. New insights into the development of brittle shear fractures from a 3-D numerical model of microcrack interaction. Earth Planet. Sci. Lett. 249, 14–28.

Healy, D., Jones, R.R., Holdsworth, R.E., 2006b. Three-dimensional brittle shear fracturing by tensile crack interaction. Nature 439, 64–67.

Hoek, E., Bieniawski, Z.T., 1965. Brittle fracture propagation in rock under compression. Int. J. Fract. 1, 137–155.

Horii, H., Nemat-Nasser, S., 1985. Compression-induced microcrack growth in brittle solids: axial splitting and shear failure. J. Geophys. Res. 90 (B4), 3105–3125.

Horii, H., Nemat-Nasser, S., 1986. Brittle failure in compression: splitting, faulting, and brittle–ductile transition. Philos. Trans. R. Soc. Lond. A 319, 337–374.

Huang, M.L., Wong, R.H.C., 2007. Experimental study on propagation and coalescence mechanisms of 3D surface cracks. Chin. J. Rock Mech. Eng. 26, 1794–1799.

Kaiser, P.K., Morgenstern, N.R., 1981. Phenomenological model for rock with time-dependent strength. Int. J. Rock Mech. Min. Sci. Geomech. Abstract 18, 153–165.

Li, L.C., Tang, C.A., Li, G., Wang, S.Y., 2012a. Numerical simulation of 3D fracture based on improved flow-stress-damage model and parallel FEM technique. Rock Mech. Rock Eng. 45, 801–818.

Li, L.C., Tang, C.A., Wang, S.Y., 2012b. Numerical investigation on fracture infilling and spacing in layered rocks subjected to hydro-mechanical loading. Rock Mech. Rock Eng. 45, 753–765.

Li, L.C., Tang, C.A., Wang, S.Y., Yu, J., 2012c. A coupled thermo-hydrologic-mechanical damage model and associated application in a stability analysis on a rock pillar. Tunneling Underground Space Technol. 34, 38–53.

Liang, Z.Z., Xing, H., Wang, S.Y., Williams, D.J., Tang, C.A., 2012. A three-dimensional numerical investigation of fracture of rock specimen containing a pre-existing surface flaw. Comput. Geotechnics 45, 19–33.

Mogi, K., 1967. Effect of intermediate principal stress on rock failure. J. Geophys. Res. 72, 5117–5131.

Place, D., Mora, P., 1999. The lattice solid model to simulate the physics of rocks and earthquakes: incorporation of friction. J. Comput. Phys. 150, 332–372.

Rutter, e.h., 1986. On the nomenclature of mode of failure transitions in rocks. Tectonophysics 122, 381–387.

Sammis, C.G., Ashby, M.F., 1986. The failure of brittle porous solids under compressive stress states. Acta Metall. 34, 511–526.

Schlangen, E., Van Mier, J.G.M., 1992. Experimental and numerical analysis of micromechanisms of fracture of cement-based composites. Cement Concr. Compos. 14 (2), 105–118.

Shen, B., Stephansson, O., 1993. Numerical analysis of mixed mode I and mode II fracture propagation. Int. J. Rock Mech. Min. Sci. Geomech. Abstract 30 (7), 861–867.

Tang, C.A., 1997. Numerical simulation of progressive rock failure and associated seismicity. Int. J. Rock Mech. Min. Sci. 34, 249–261.

Tang, C.A., Kou, S.Q., 1998. Crack propagation and coalescence in brittle materials under compression. Eng. Fract. Mech. 61, 311–324.

Tang, C.A., Lin, P., Wong, R.H.C., Chau, K.T., 2001. Analysis of crack coalescence in rock-like materials containing three flaws-Part II: numerical approach. Int. J. Rock Mech. Min. Sci. 38, 925–939.

Tang, C.A., Tham, L.G., Wang, S.H., Liu, H., Li, W.H., 2007. A numerical study of the influence of heterogeneity on the strength characterization of rock under uniaxial tension. Mech. Mater. 39, 326–339.

Tien, Y.M., Kuo, M.C., Juang, C.H., 2006. An experimental investigation of the failure mechanism of simulated transversely isotropic rocks. Int. J. Rock Mech. Min. Sci. 43, 1163–1181.

Turcotte, D.L., Newman, W.I., Shcherbakov, R., 2003. Micro and macroscopic models of rock fracture. Geophys. J. Int. 152, 718–728.

Vasarhelyi, B., Bobet, A., 2000. Modeling of crack initiation, propagation and coalescence in uniaxial compression. Rock Mech. Rock Eng. 33 (2), 119–139.

Wang, S.Y., Lam, K.C., Au, S.K., Tang, C.A., Zhu, W.C., Yang, T.H., 2006. Analytical and numerical study on the pillar rockbursts mechanism. Rock Mech. Rock Eng. 39 (5), 445–467.

Wang, S.Y., Sun, L., Au, A.S.K., Yang, T.H., Tang, C.A., 2009. 2D-numerical analysis of hydraulic fracturing in heterogeneous geo-materials. Constr. Build. Mater. 23 (6), 2196–2206.

Wang, S.Y., Sloan, S.W., Huang, M.L., Tang, C.A., 2011a. Numerical study of failure mechanism of serial and parallel rock pillars. Rock Mech. Rock Eng. 44 (2), 179–198.

Wang, S.Y., Sloan, S.W., Liu, H.Y., Tang, C.A., 2011b. Numerical simulation of the rock fragmentation process induced by two drill bits subjected to static and dynamic loading. Rock Mech. Rock Eng. 44 (3), 317–332.

Wang, S.Y., Sloan, S.W., Sheng, D.C., Tang, C.A., 2012a. Numerical analysis of the failure process around a circular opening in rock. Comput. Geotech. 39, 8–16.

Wang, S.Y., Sloan, S.W., Tang, C.A., Zhu, W.C., 2012b. A numerical investigation of the failure mechanism around tunnels in transversely isotropic rock masses. Tunneling Underground Space Technol. 32, 231–244.

Weibull, W., 1951. A statistical distribution function of wide applicability. J. Appl. Mech. 18, 293–297.

Wong, R.H.C., Chau, K.T., 1998. Crack coalescence in a rock-like material containing two cracks. Int. J. Rock Mech. Min. Sci. 35, 147–164.

Wong, R.H.C., Chau, K.T., Tang, C.A., Lin, P., 2001. Analysis of crack coalescence in rock-like materials containing three flaws-Part I: experimental approach. Int. J. Rock Mech Min. Sci. 38, 909–924.

Xu, T., Tang, C.A., Zhao, J., Li, L., Heap, M.J., 2012. Modelling the time-dependent rheological behaviour of heterogeneous brittle rocks. Geophys. J. Int. 198, 1781–1796.

Yang, S.Q., Jiang, Y.Z., Xu, W.Y., Chen, X.Q., 2008. Experimental investigation on strength and failure behaviour of pre-cracked marble under conventional triaxial compression. Int. J. Solids Struct. 45, 4796–4819.

Yang, S.Q., Jing, H.W., Wang, S.Y., 2012a. Experimental study on the strength, deformability, failure behaviour and spatial acoustic emission distribution of red sandstone under triaxial compression. Rock Mech. Rock Eng. 45, 583–606.

Yang, S.Q., Yang, D.S., Jing, H.W., Li, Y.H., Wang, S.Y., 2012b. An experimental study of the fracture coalescence behaviour of brittle sandstone samples containing three fissures. Rock Mech. Rock Eng. 45, 563–582.

Yu, M.H., 2004. Unified Strength Theory and Its Applications. Springer-Verlag, Berlin.

Zhu, W.C., Tang, C.A., 2006. Numerical simulation of Brazilian disk rock failure under static and dynamic loading. Int. J. Rock Mech. Min. Sci. 43, 236–252.

Zhu, W.S., Chen, W.Z., Shen, J., 1998. Simulation experiment and fracture mechanism study on propagation of Echelon pattern cracks. Acta Mech. Solida Sin. 19, 355–360 (in Chinese).